Journal of Zhejiang University-SCIENCE A in press
www.jzus.zju.edu.cn; www.springer.com/journal/11582
E-mail: jzus_a@zju.edu.cn

Research Article
https://doi.org/10.1631/jzus.A2500625

Rapid, material-aware inverse design of one-dimensional photonic crystals using a mixture-of-physics-expert framework

Haoming LI*, Zhiyuan ZHOU*, Xinzi LIN, Wuyong QU, Dongxu JI✉

School of Science and Engineering, The Chinese University of Hong Kong, Shenzhen, Shenzhen 518172, China

Abstract: In this work, we present an unsupervised physics-informed neural network (PINN) framework for the inverse design of one-dimensional photonic crystals, addressing the limitations of conventional methods, such as high computational cost and inability to optimize materials. A "mixture-of-physics-experts" method for nanophotonic design is proposed, which pretrains a library of PINN models for various material combinations. This allows for not only rapid structure optimization directly from target spectra, even hand-drawn ones but also efficient selection of the optimal material system for a given task, a capability traditional algorithms lack. By embedding physical governing equations as a loss constraint, our framework eliminates the need for large labeled datasets and enhances physical explainability. As a practical demonstration, we apply this framework to design a spectral-splitting optical filter for a high-bandgap/low-bandgap hybrid photovoltaic system. We compare designs from five pretrained material-specific PINN models and identify the optimal material configuration that enhances the overall PV system efficiency by 22.4% compared with a standalone GaAs solar cell and 41.9% compared with a GaInP cell. Notably, the designed filters exhibit excellent angular robustness with only 3.5% relative efficiency degradation at 45° oblique incidence and significantly reduce the operating temperature of low-bandgap cells by 12.8–14.6°C. This physics-guided, material-aware framework establishes a new paradigm for photonic device design, balancing computational efficiency, design flexibility, and practical applicability.

Key words: Photonic Crystals; Physics-informed Neural Network; Genetic Algorithm; Thin Film.

1 Introduction

Multilayer one-dimensional photonic crystals (1D-PhCs) are vital in optics and energy engineering(Li et al., 2024, Yu et al., 2025, Li et al., 2025). 1D-PhCs operate by introducing a structure with periodic variation in the refractive index along a single spatial dimension, therefore enabling precise control over the light flow(Wan. et al., 2021). This capability has made 1D-PhCs indispensable in a variety of applications, including optical filters for thermophotovoltaics(Ma et al., 2025), spectral splitting for photovoltaic systems(Qu et al., 2025), and biosensing(Pavlichenko et al., 2015). Effective design of a 1D-PhC that features a required behavior involves exploring a vast parameter space, including material choices, layer thicknesses, and refractive index contrasts. The high level of flexibility poses a significant challenge for the inverse design methodology of 1D-PhC(Luce et al., 2023).

Traditional inverse design for nanophotonics relies heavily on gradient-based approaches or evolutionary optimization(Molesky et al., 2018). The core principle of these traditional methods is defining and using a physics-based forward model to guide the optimization. For instance, the Transfer Matrix Method (TMM)(Hecht, 2021, Luce et al., 2022) is a typical physics-based forward model. This model takes the PhC parameters, such as refractive indices and thicknesses of layers, as input and outputs the response spectrum of the current PhC structure. The iterative gradient descent method(Anzengruber et al., 2012) calculates the gradient of the PhC's response spectrum with respect to the refractive index distribution and uses the gradient to minimize the difference between the PhC

✉ Dongxu JI, jidongxu@cuhk.edu.cn
* The two authors contributed equally to this work

Received Nov. 29, 2025; Revision accepted Mar. 16, 2026; Crosschecked

design's response spectrum and the target spectrum. The main drawbacks of the iterative gradient descent method are local optima and high computational cost. In contrast, heuristic optimization algorithms such as the genetic algorithm (GA)(Schubert et al., 2008, Liu et al., 2024), particle swarm optimization (PSO)(Ruan et al., 2016, Lee et al., 2023) and needle method(Tikhonravov et al., 1996, Tikhonravov et al., 2007) have better global optimization capabilities, effectively overcoming local optima entrapment while exploring the design space. Apart from merely optimizing the PhC structure, the GA can also inversely design the material and total layer number (Kim et al., 2021). Nevertheless, the traditional methods are more suitable for the "one-task-one-calculation" scenario. They require starting from scratch for each task, and the computational cost of heuristic optimization algorithms remains prohibitively high, especially for inverse design tasks involving 1D-PhCs with numerous layers. Predicting structures that generate a spectrum sufficiently matching the target spectrum within a reasonable time becomes difficult or even practically infeasible(Zhan et al., 2022, Lininger et al., 2021). Hence, a fast and adaptable inverse design method is needed for more complicated 1D-PhC design tasks.

Compared with traditional inverse design methods, the artificial intelligence (AI) method enables higher computational efficiency(Wang et al., 2024). A variety of deep learning methods have been applied to efficiently solve the inverse design problem of 1D-PhCs, such as fully connected networks (FCNs)(Liu et al., 2018), convolutional neural networks (CNNs)(Lininger et al., 2021), conditional invertible neural networks (cINNs)(Luce et al., 2023), variational autoencoders (VAEs)(Hong and Nicholls, 2022), and transformers(Ma et al., 2024). Nevertheless, the deep learning methods mentioned above are based on purely data-driven supervised learning, which suffers from two major limitations: a) reliance on extensive labeled datasets comprising real-world spectral data and photon crystal structures and b) the absence of physical explainability. To obtain an efficient deep learning model, the researcher must generate numerous 1D-PhC structures as the training labels (ground truths) alongside their corresponding optical response spectra as the training data. Thousands to tens of millions of real-world structures and spectra are typically used to train the models in previous relevant studies, which leads to a significantly large computational cost(Hong and Nicholls, 2022, Lininger et al., 2021, Luce et al., 2023, Ma et al., 2024). Moreover, it has been widely reported that models trained on real-world datasets struggle with tasks beyond their training domain, particularly in tasks of inverse PhC design, where target spectra are often idealized step-like profiles that do not exist in either practical scenarios or real-world training datasets(Wang et al., 2021, Luce et al., 2023, Wang et al., 2024). This mismatch between the training datasets and tasks significantly limits the performance and generalization ability of the data-driven model. Another critical issue of traditional data-driven deep learning models is the black box problem(Pedreschi et al., 2019), which suggests that the current data-driven deep learning models lack physical explainability.

To address the above problem of traditional data-driven AI models, many studies have advocated for the adoption of more explainable AI models(Jiménez-Luna et al., 2020, I. et al., 2022, Wang et al., 2022). As a type of explainable AI model, the physics-informed neural network (PINN) has been introduced in various recent studies(Zhelyeznyakov et al., 2023, Khatib et al., 2022, Riganti et al., 2025, Medvedev et al., 2025, Chen and Dal Negro, 2022, Chen et al., 2020, Zhu et al., 2025) to solve optical inverse problems. Unlike pure data-driven models that depend on labels, PINNs integrate physical governing equations as regularization constraints during training, effectively embedding prior physics knowledge into the optimization process through residual loss functions(Medvedev et al., 2025). This strategy significantly enhances the prediction accuracy and accelerates the network convergence in intelligent metasurfaces(Qian et al., 2024). The adoption of physical constraints reduces the parameter search space and guides gradient backpropagation in network training, allowing neural networks to learn complex mappings with less reliance on large amounts of data. Furthermore, the PINN(Khatib et al., 2022) achieves a significantly lower error compared to the traditional data-driven network in

electromagnetic response prediction tasks that fall outside the training data distribution space, with a reduction of 36% in parameter scale compared to a traditional data-driven network.

To demonstrate the practical utility of our framework, we apply it to design spectral-splitting filters for hybrid photovoltaic systems. While single-junction cells face fundamental Shockley-Queisser efficiency limits (Rühle, 2016), multijunction architectures suffer from current-matching constraints and fabrication complexity that compromise reliability (Rahman et al., 2025). Spectral-splitting photovoltaic (SSPV) systems circumvent these issues by spatially separating subcells to absorb specific spectral bands without electrical interconnection (Dorodnyy et al., 2015; Zhu. et al., 2015; Jiang et al., 2019; Ahmadi et al., 2025). However, existing SSPV filter designs rely on computationally expensive iterative optimizations. We address this bottleneck by developing a differentiable transfer matrix method (TMM) that embeds physical laws directly into PINN training without requiring labeled data. Our key innovation is a "Mixture-of-Physics-Experts" (MOPE) strategy, which is analogous to a mixture-of-experts (MOE) model in the large language model field. We pretrain specialized PINN models for distinct material combinations, conduct parallel inference of the PINN model, and choose the best material combination and PhC structure, enabling rapid material-system selection and structure optimization that traditional algorithms cannot achieve.

2 Methodology

The inverse design problem can be formulated as an input-output mapping. As shown in Fig. 1(a) and Fig. 2, the model takes the target reflectance spectrum as the input and predicts the corresponding 1D-PhC structure as the output. The structure is represented as an l-dimensional vector $\boldsymbol{d} = [d_1, d_2, \ldots, d_l]$, where d_n is the thickness of the nth layer and l is the number of layers. The target spectrum is a vector $\boldsymbol{r} = [r_1, r_2, \ldots, r_k]$ containing the reflectance values at k wavelength sampling points, as shown in Fig. 1(a). Three cases were conducted in this study to comprehensively evaluate the performance of the proposed PINN framework: Case 1 compares PINN and data-driven CNN training using a real-world dataset of TiO_2-SiO_2 structures; Case 2 evaluates eight PINN models with different material combinations on various optical filter design tasks; Case 3 applies the MOPE framework to design spectral-splitting filters for hybrid PV systems. The detailed experimental setup for each case is described in section 3. Fig. 1(b) illustrates the concept of the SSPV system. Incident sunlight first encounters the 1D-PhC dichroic filter, which functions as a spectral beam splitter. The filter is designed to transmit photons with wavelengths shorter than the cutoff wavelength to the high-bandgap cell (GaAs or GaInP) while reflecting photons with wavelengths longer than the cutoff wavelength to the low-bandgap cell (Si). The high- and low-bandgap cells are spatially separated from each other, and they are electrically isolated, with no series or parallel connections between their respective electrode terminals. This spectral separation strategy enables each photovoltaic cell to operate within its optimal spectral range, minimizing thermalization losses in the high-bandgap cell and sub-bandgap transmission losses in the low-bandgap cell. The combined system thus achieves higher overall efficiency than either standalone cell alone.

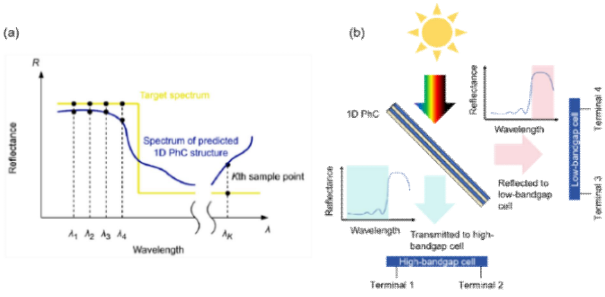

Fig. 1 (a) An example of the sampling of the ideal target spectrum (yellow line) and spectrum of the predicted 1D-PhC structure (blue curve). (b)Illustration of the concept of a spectral-splitting photovoltaic system.

2.1 Neural network structure

The structure of the PINN model in this study is based on a typical convolutional architecture shown in Fig. 2. The network consists of two parts: the feature learning part and the numerical regression part. The feature learning part accepts the input target spectrum (vector $\boldsymbol{r}$), with convolutional layers

and maxpooling layers alternating in a sequential manner to extract a series of features from the target spectrum while reducing spatial dimensions. The regression part performs numerical regression to predict the thickness of each layer in the 1D-PhC. Specifically, after flattening the feature maps from the last layer of the feature learning component into a one-dimensional vector, a series of fully connected layers maps these features to the desired output dimensions. The final layer outputs a one-dimensional vector $\boldsymbol{d}_\mathrm{p}$ representing the thicknesses of individual layers in the 1D-PhC.

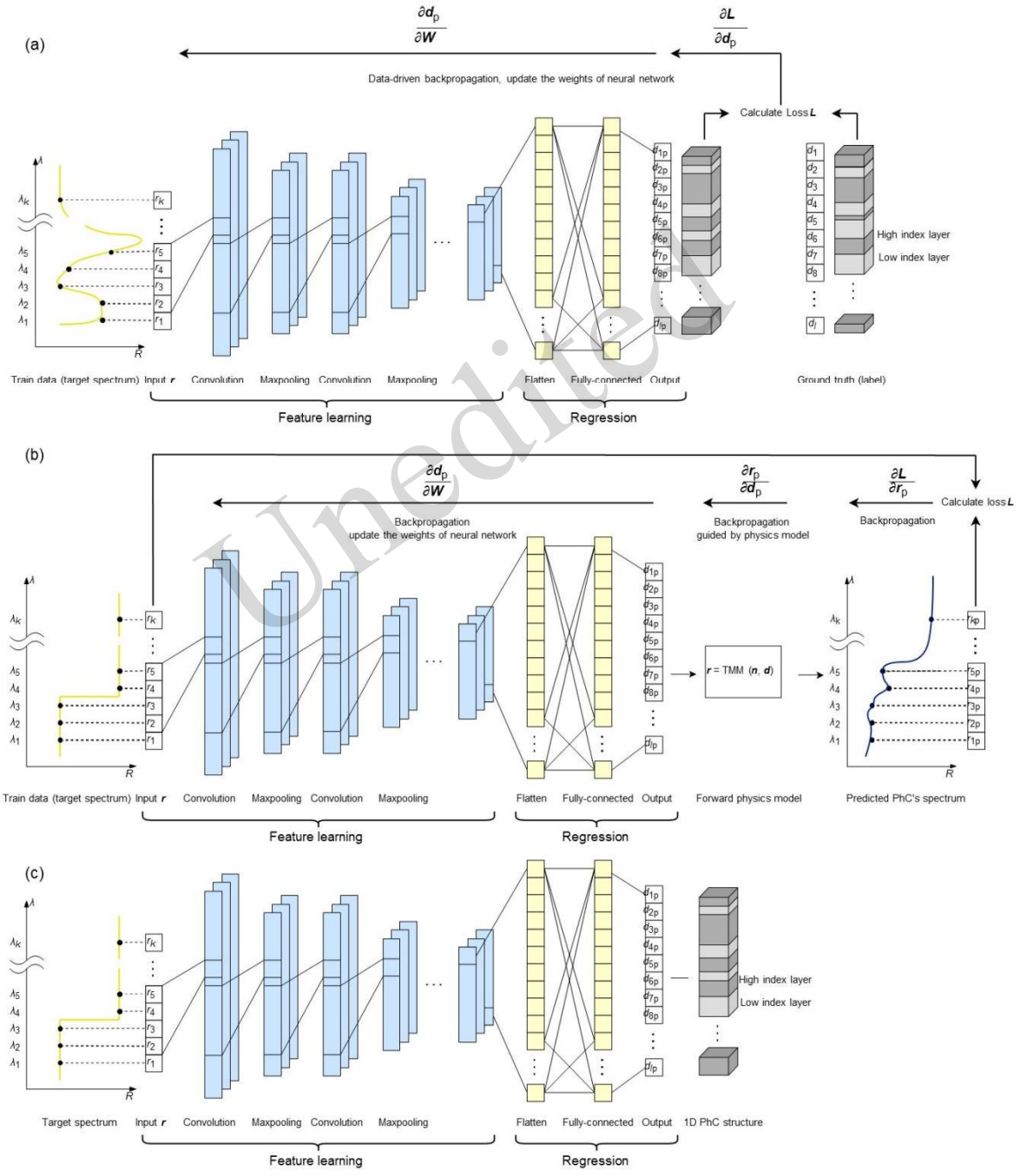

Fig. 2. (a) Supervised data-driven training of CNN. (b) Unsupervised training of the PINN. (c) Inference of the PINN or CNN

2.2 PINN Training

In the training process, as shown in Fig. 2(b), we use the ideal spectra as the training data, and the model predicts the structure of the 1D-PhCs corresponding to these spectra. Then, a differentiable forward physics model mentioned above takes the predicted structures $\boldsymbol{d}_\mathrm{p}$ and calculates their response spectra $\boldsymbol{r}_\mathrm{p}$:

$$\boldsymbol{r}_\mathrm{p} = \mathrm{TMM}(\boldsymbol{n}, \boldsymbol{d}_\mathrm{p}) \quad (1)$$

where TMM is the differentiable forward physics model, $\boldsymbol{n}$ is the vector of preset refractive indices of the PhC layers, which correspond to the preset film material configuration, and $\boldsymbol{d}_\mathrm{p}$ represents the vector of predicted 1D-PhC layer thicknesses.

The loss function for PINN training can be described as

$$\boldsymbol{L} = \alpha \cdot \boldsymbol{L}_\mathrm{MSE} + \beta \cdot \sum_{i=1}^{11} \boldsymbol{L}_{\mathrm{reg,\ i}} \quad (2)$$

where $\boldsymbol{L}_\mathrm{MSE}$ represents the mean square error (MSE) between the input ideal spectra $\boldsymbol{r}$ and the spectra of the predicted 1D-PhC structure, $\boldsymbol{r}_\mathrm{p} = [r_{1\mathrm{p}}, r_{2\mathrm{p}}, r_{3\mathrm{p}}, \ldots, r_{k\mathrm{p}}]$, $\boldsymbol{L}_{\mathrm{reg,i}}$ denotes the regulation for restraining the thickness of each layer within the range of 0.02-0.3 μm, and α and β are the weight coefficients. The regulation loss function can be found in the supporting information.

The $\boldsymbol{L}_\mathrm{MSE}$ is calculated by

$$\boldsymbol{L}_\mathrm{MSE} = \frac{1}{B}\sum_{b=1}^{B}\frac{1}{K}\sum_{k=1}^{K}\left(r_{k\mathrm{p}}^{b} - r_{k}^{b}\right)^2 \quad (3)$$

where B and b are the batch size and the ordinal number of data in the mini batch, respectively. K is the number of wavelength sample points on the spectra and is fixed to 161 in this work. $r_{k\mathrm{p}}$ represents the reflectance value of the kth sample point of the predicted 1D-PhC spectrum, and r_k is the reflectance value of the kth sample point of the input spectrum. Unlike conventional data-driven approaches requiring explicit ground-truth structures as labels and corresponding spectra as training data, the PINN method utilizes input spectra dually as both training data and labels. Crucially, these training spectra accommodate both experimentally measured data (with known physical structures) and idealized forms, including analytically defined curves. This dual functionality offers flexibility in training data acquisition and better generalization ability. The backpropagation and PINN weight update follow the equation of

$$\frac{\partial \boldsymbol{L}}{\partial \boldsymbol{W}} = \frac{\partial \boldsymbol{L}}{\partial \boldsymbol{r}_\mathrm{p}} \cdot \frac{\partial \boldsymbol{r}_\mathrm{p}}{\partial \boldsymbol{d}_\mathrm{p}} \cdot \frac{\partial \boldsymbol{d}_\mathrm{p}}{\partial \boldsymbol{W}} \quad (4)$$

where $\boldsymbol{W}$ represents the neural network weights. The physics model guides the gradient backpropagation, as shown in Fig. 2(b), and details about the differentiable forward physics model can be found in the supplementary information.

2.3 Data-driven CNN Training

A CNN model is trained in parallel using the data-driven training method to compare with the PINN model. The neural network structure of the CNN is the same as that of the PINN, and the training method is illustrated in Fig. 2(a). A large number of 1D PhC structures ($\boldsymbol{d}$) are generated as the training label, and their corresponding reflectance spectra (r) are obtained as the input training data.

The loss function of CNN training is defined as

$$\boldsymbol{L} = \gamma \cdot \frac{1}{B}\sum_{b=1}^{B}\frac{1}{l}\sum_{i=1}^{l}\left(d_{i\mathrm{p}}^{b} - d_{i}^{b}\right)^2 + \delta \cdot \sum_{i=1}^{11} \boldsymbol{L}_{\mathrm{reg,\ i}} \quad (5)$$

where i is the ordinal number of the 1D-PhC layer, $d_{i\mathrm{p}}$ is the predicted thickness of the ith layer, and d_i is the true thickness of the ith layer in the label. γ and δ are the weight coefficients. l is the total number of layers in the 1D PhC, which is set to 11 or 9 in this study. The regulation function for CNN training is the same as that for PINN training, which is described in the supporting information. The training hyperparameters are set to be consistent for both the PINN and CNN to ensure the fairness of the comparison. The detailed training settings are listed in the supporting information.

3 Experimental design and data preparation

Three cases were conducted in the experiment to analyze the performance of the CNN and PINN methods.

Case 1: The data-driven CNN and PINN were trained, validated and compared based on the same real-world dataset to analyze the impact of physics information on the training process. A real-world dataset was constructed, including 12800 randomly generated 11-layer TiO_2-SiO_2 periodic 1D-PhC

structures and their corresponding reflectance spectra calculated by TMM. The thickness of each layer in the randomly generated structures was set to range from 0.02 to 0.3 μm. The dataset was split into training data (80%, 10240 pairs of 1D-PhC structure and spectra), validation data (12%, 1536 pairs of 1D-PhC structure and spectra), and test data. The performance of both models was evaluated in each training epoch by predicting the 1D-PhC structures corresponding to the validation spectra, feeding the predicted structures into TMM to compute the reflectance spectra, and recording the mean absolute error (MAE) between the predicted and ground-truth spectra. The convergence behavior of each method during training was monitored based on the calculated MAE.

Case 2: Eight PINN models with eight distinct material combinations were trained to investigate the material-dependent predictive capabilities of the proposed model. 1D-PhCs typically feature periodic structures composed of materials with varying refractive indices. While some studies use only two materials (e.g., high-low refractive index pairs), others employ multiple material configurations. In this experiment, eight commonly used material configurations were selected: TiO_2-Al_2O_3, TiO_2-SiO_2, Ta_2O_5-SiO_2, Ta_2O_5-Al_2O_3, TiO_2-Ta_2O_5, Al_2O_3-SiO_2, TiO_2-Ta_2O_5-Al_2O_3-SiO_2, and TiO_2-SiO_2-Ta_2O_5-Al_2O_3. Specific material sequences can be found in the supporting information section.

The training data in case 2 were a group of ideal spectra, such as the yellow spectrum in Figure 1. The total number of ideal spectra for training was 2250. All eight models were trained based on the same group of ideal spectra. Posttraining evaluations were conducted by employing these models for eight distinct inverse design tasks, such as optical longpass filters, band notch filters, bandpass filters, and shortpass filters. The target spectra of the tasks were independent of the training data.

Case 3: Application in Spectral-Splitting Photovoltaic System Design. To demonstrate the practical utility of the MOPE framework, we tasked our pretrained models with a real-world challenge: designing a 9-layer spectral-splitting filter for a spectral-splitting PV system. We selected five promising material combinations from the library: TiO_2-Al_2O_3-MgF_2 (TAM), TiO_2-Al_2O_3 (TA), TiO_2-MgF_2 (TM), TiO_2-SiO_2-MgF_2 (TSM), and TiO_2-SiO_2 (TS). The detailed material configurations are listed in the supporting information section. Each corresponding PINN model was used to inversely design a filter structure based on ideal spectral-splitting target spectra. The performance of these uniquely designed filters was then evaluated by simulating their impact on the total power output of two different tandem PV systems: a GaAs/Si system and a GaInP/Si system. This case is designed to showcase our method's ability to not only generate device structures rapidly but also to facilitate the selection of the best material system for a specific application by comparing end-to-end system performance. The performances of GaAs and Si cells are calculated by the single-diode model, while GaInP is simulated by the double-diode model since the single-diode parameters of GaInP cells are rarely reported in the literature, and the single-diode or double-diode parameters of Si, GaAs and GaInP cells utilized in this work are listed in the supporting section. The current-voltage (J-V) curves can be calculated by the diode models, and the maximum power point can be found on the J-V curves. Then, the output power from each cell can be calculated. The detailed calculation process of the single- and double-diode models can be found in the supporting material as well.

4 Results and discussion

4.1 Case 1: impact of physics information in model training

As discussed in the methodology section, the differentiable TMM is used as a part of the loss function to train the PINN model. In contrast, the loss function of the data-driven models only consists of the regulation of layer thicknesses and the MSE between the predicted PhC layer thicknesses and the target thicknesses. The mean absolute error between the predicted 1D PhC structure spectra and the target spectra every 50 epochs is shown in Fig. 3. This indicates that the validation loss of the PINN decreases rapidly from approximately 0.312 to 0.130 during the 0-100 epochs and then converges at approximately 0.121 after epoch 650, whereas the validation loss of the data-driven CNN decreases more slowly, converging at approximately 0.269

after epoch 950. At the end of the training, the validation loss of the PINN is 0.121, which is 54.5% lower than that of the data-driven CNN, with a validation loss of 0.266.

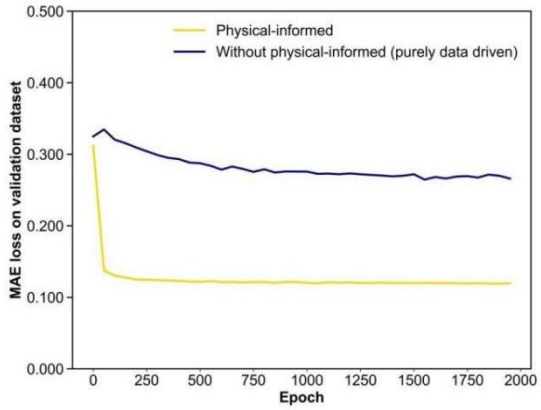

Fig. 3. Comparison of the validation losses of the PINN and data-driven CNN during the training process.

The better convergence behavior and prediction accuracy of the PINN model can be attributed to two key mechanisms that fundamentally differentiate it from the data-driven CNN. First, integrating the differentiable TMM as a physics-informed constraint during backpropagation introduces a directional guidance mechanism for gradient updates. This physical model acts as a prior knowledge layer, effectively narrowing the weight search space by aligning the optimization trajectory with the intrinsic electromagnetic response characteristics of 1D-PhC structures. In contrast, the weights of the CNN are updated based on a purely data-driven "trial-and-error" mechanism. Second, the PINN directly uses the response spectrum in the training data as the training target, bypassing the need for intermediate structural labels. The end-to-end, target-oriented approach of PINN ensures that the predicted 1D-PhC structures prioritize matching the desired optical response over pursuing structural features, leading to higher accuracy. These advantages collectively explain why the PINN achieves a 54.5% lower validation loss than the data-driven model. In contrast, the CNNs' reliance on layer thickness regulation as an indirect surrogate for spectral control may compromise precision.

4.2 Case 2: material-dependent predictive capabilities

As shown in Fig. 4, eight models with different groups of materials were used to predict the 1D-PhC structures from eight ideal target reflectance spectra: Task 1/2: bandpass (short/long cutoff wavelength); Task 3/4: longpass (short/long cutoff wavelength); Task 5/6: band notch (short/long cutoff wavelength); and Task 7/8: shortpass (short/long cutoff wavelength).

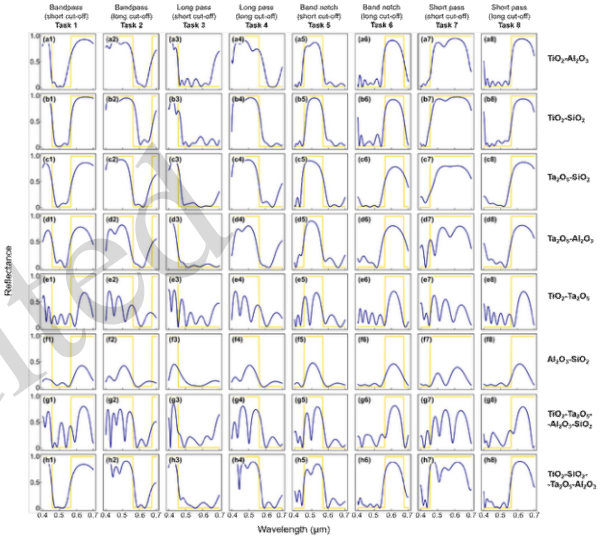

Fig. 4. Performance comparison of eight models trained with distinct material configurations: predicted vs. target reflectance spectra of 1D-PhCs (blue curves: model predicted structures' spectra, yellow lines: target spectra)

The eight target spectra were carefully chosen to cover the majority of representative optical filters. The similarity between the predicted 1D-PhC structure's reflectance spectrum and the target spectrum reveals the model's performance on the particular task. For instance, it can be easily inferred from Fig. 4(f1-f8) that the Al_2O_3-SiO_2 model is unsuitable for all 8 tasks since the peak intensities of the response spectra are below 0.5, whereas the value of the target spectra at the same wavelength is 1, and the spectral bandwidths of the peaks are also narrower than those of the target spectra. This finding is consistent with expectations. According to dielectric film theory(Hecht, 2021), the achievable reflectance and peak spectral bandwidth are fundamentally constrained by the difference between material refractive indices; therefore, the limited refractive index difference between the high-index material (Al_2O_3, n_H ~ 1.62) and low-index material

(SiO_2, n_L ~ 1.46) results in an intrinsic performance limitation. In contrast, it is observed that the TiO_2-SiO_2 model, as shown in Fig. 4(b1-b8), has a satisfying response spectrum on the tasks among all material combinations because the refractive index difference between TiO_2 (n_H ~ 2.38) and SiO_2 (n_L ~ 1.46) is highest among all eight preset material models. Nevertheless, some models have generated similar response spectra on the same task, such as Fig. 4(b3) and Fig. 4(c3), and the model performances cannot be evaluated solely by overlooking the spectra.

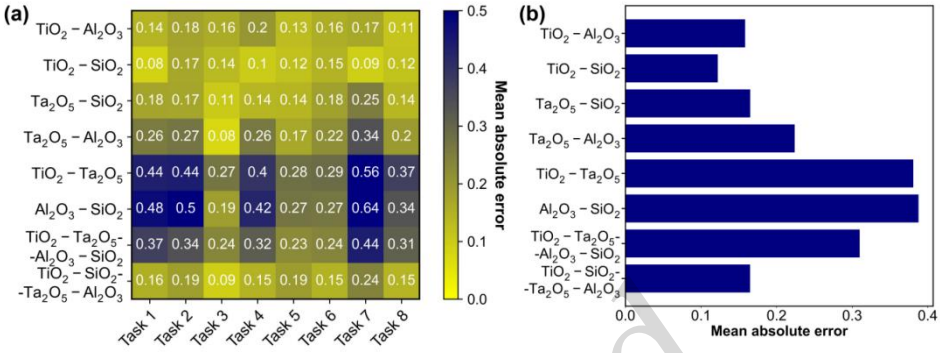

Fig. 5. (a) Heatmap of MAEs between predicted and target spectra for 1D-PhCs across 8 preset material models (y-axis) and 8 spectral-design tasks (x-axis). (b) Average MAEs between predicted and target spectra for 1D-PhCs, calculated across all 8 spectral-design tasks.

To further distinguish the predictive capabilities of eight preset material models, the model performance is further quantified by calculating the MAEs between the predicted and target spectra, and the results are presented in Figure 5. The TiO_2-SiO_2 model achieves the lowest MAEs among all preset material models on nearly all inverse design tasks, apart from the longpass (short cutoff wavelength) task. The average MAEs of the TiO_2-SiO_2 and Al_2O_3-SiO_2 models are 0.12 and 0.39, respectively, representing the best and worst predictive performances among all preset material models. Notably, neither the TiO_2-Ta_2O_5-Al_2O_3-SiO_2 model nor the TiO_2-SiO_2-Ta_2O_5-Al_2O_3 model exhibits better overall performance than the TiO_2-SiO_2 model, and their MAEs are 0.31 and 0.17, respectively, despite having more varied material collocations. These findings reveal that the diversification of material combinations in some inverse design problems may not necessarily lead to improved performance. Therefore, the combination of TiO_2 and SiO_2 alone may suffice for achieving comparable performance in inverse design problems within the visible light spectrum.

Additionally, an interesting pattern is noted in Figure 5(a) that several inverse design tasks, such as longpass (short cutoff wavelength) and band notches, are relatively easy for nearly all preset material models. The average MAEs across all models for these 3 tasks are 0.16, 0.19, and 0.21, respectively. A possible explanation is that the target spectra of these tasks feature a significantly higher proportion of regions where the reflection coefficient is 0, which reduces the difficulty for the models in predicting appropriate 1D-PhC structures. Another observation, contrarily, supports our previous explanation. The shortpass (short cutoff wavelength) task, which exhibits the largest proportion of reflectance = 1 spectral region among all tasks, is proven to be the most challenging for all preset materials models, leading to one of the highest average MAEs of 0.34. Nevertheless, the preset TiO_2-SiO_2 model reaches a considerably low MAE of 0.09 for this inverse design task. This finding further validates our earlier conclusion that the combination of TiO_2 and SiO_2 may be adequate for most tasks within the 400-700 nm spectral band.

4.3 Case 3: Design of optical filters for an SSPV system

After validating the efficiency of the PINN approach and demonstrating its capability in handling various material systems, we now apply our framework to a practical engineering problem: designing a dichroic filter for a spectral-splitting photovoltaic system. In this case, five different sets of material configurations are selected to design an

optic filter for combined PV cells. The cutoff wavelength is adjustable to match different combined cells. The first system utilized a GaAs/Si system, requiring the filter's cutting wavelength to be set near 0.86 μm. The second system, leveraging the wider bandgap of GaInP, employed a GaInP/Si structure, for which the filter's cutting wavelength was 0.72 μm. To fairly evaluate the system performance under practical operating conditions, simulations are conducted at both normal incidence (0°) and oblique incidence (45°), the latter representing the actual operating angle for the dichroic splitter in the spectral-splitting configuration shown in Fig. 1(b).

4.3.1 GaAs/Si System Performance

Analysis of the predicted reflectance spectra for the GaAs/Si system at 0° incidence (Fig. 6) reveals distinct performance characteristics among the five material combinations. Notably, the filters designed using TiO_2-Al_2O_3 (TA1) and TiO_2-SiO_2 (TS1) exhibit exceptionally sharp transitions at the cutoff wavelength, which is critical for efficient spectral separation. A critical observation is the behavior of the reflectance in the long-wavelength regime. Unlike the other four sets, which maintain a high reflectance close to the ideal value, set TiO_2-Al_2O_3 exhibits a distinct roll-off in reflectance, as shown in Fig. 6(b). One possible reason for this phenomenon is that the refractive index difference between TiO_2 and Al_2O_3 is the smallest among these combinations of materials. This performance degradation is attributed to the lower refractive index contrast between TiO_2 (n ~ 2.3) and Al_2O_3 (n ~ 1.7) compared to other pairs such as TiO_2/SiO_2 (n ~ 1.46), which limits the achievable stopband width and reflectance according to thin-film theory.

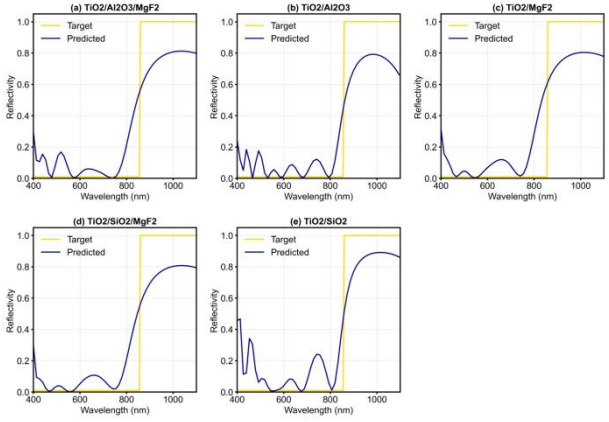

Fig. 6. Performance comparison of five models trained with distinct material configurations: the GaAs/Si system. The reflectance spectra at an incident angle of 0 degrees for (a) TiO_2-Al_2O_3-MgF_2 (TAM1), (b) TiO_2-Al_2O_3 (TA1), (c) TiO_2-MgF_2 (TM1), (d) TiO_2-SiO_2-MgF_2 (TSM1), and (e) TiO_2-SiO_2 (TS1).

The J-V curves of the GaAs/Si system under 0° incidence are presented in Fig. 7. The most significant change compared with the reference curves in Fig. 7(f) is observed in the Si cell. Both the short-circuit current density and the open-circuit voltage of the Si cell are substantially reduced across all filtered configurations in Fig. 7(a)-(e). This performance drop is fundamentally attributed to the Si cell only receiving the reflected portion of the solar spectrum after the light reaches the filter. In addition, the filter in Fig. 7(b) resulted in the lowest short-circuit current density of the Si cell; this poor performance strongly correlates with its spectral response, which exhibited roll-off in the long-wavelength region, as Fig. 6(b) shows. Since the Si cell relies on the reflected portion of the spectrum, the pronounced drop in filter reflectance directly translates to a critically reduced photon flux density transmitted to the Si absorber, consequently curtailing its output current.

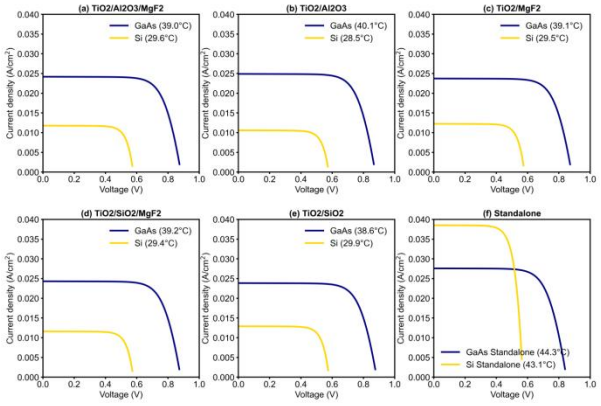

Fig. 7. J-V Curves of GaAs/Si combined solar cells under AM1.5G conditions using different spectrum splitters: (a) TiO_2-Al_2O_3-MgF_2 (TAM1) (b) TiO_2-Al_2O_3 (TA1) (c) TiO_2-MgF_2 (TM1) (d) TiO_2-SiO_2-MgF_2 (TSM1) (e) TiO_2-SiO_2 (TS1) (f) Standalone J-V curves of GaAs and Si as a reference.

For the GaAs part, a marginal decrease in performance, particularly in short-circuit current, is also evident compared with the independent operation shown in Fig. 7(f). This minor degradation stems from the fact that the filter's reflectance in the intended transmission band is not perfectly zero, as

presented by the spectral oscillations in Fig. 6. A comparison among the material configurations reveals that TS1 achieves the most favorable overall performance at 0° incidence, yielding a total power density of 0.0211 W/cm^2. This superior performance can be directly attributed to the filter's spectral characteristics shown in Fig. 6(e). First, the filter exhibits an extremely sharp transition at the band edge. Second, the filter achieves the highest reflectance in the reflection band (long-wavelength region) compared to the other configurations. Furthermore, to evaluate the angular robustness of the designed filters, we extended our analysis to 45° incidence, and the filters' reflectance spectra and the systems' J-V curves with a 45° light incidence angle can be found in the supplementary information (Fig. S7-8).

The total power density comparison for the GaAs/Si system is summarized in Fig. 8, which presents results for both 0° (Fig. 8a) and 45° (Fig. 8b) incidence angles. A crucial finding is that the implementation of the spectral splitting approach leads to a clear performance enhancement at both incidence angles, as the total power densities for all five hybrid systems surpass the power output of both the standalone GaAs and standalone Si reference cells. This confirms the efficacy of spectral splitting for improved energy harvesting and, importantly, demonstrates the robustness of the system against variations in the incident angle. The relatively modest decrease in total efficiency from 0° to 45° (approximately 3.5% for TS1) indicates that the designed filters possess excellent angular tolerance, a critical requirement for practical deployment.

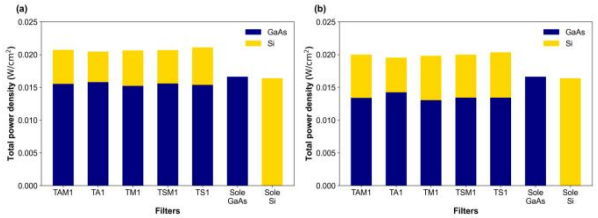

Fig. 8. Total output power density (W/cm²) of the GaAs/Si combined system using different spectral splitting filters with 0 (a) and 45 (b) degree solar incident to the splitter.

4.3.2 GaInP/Si System Performance

For the GaInP/Si system, the fundamental spectral characteristics of the five reoptimized filters remain broadly similar to the previous set designed for GaAs/Si. However, two main spectral features stand out. First, unlike the previous set, all five configurations now exhibit a universal reflectance roll-off in the far long-wavelength region. Second, regarding the key performance metric of spectral separation, the filters in Fig. 9(c) and (d) (TM2 and TSM2) achieve the most desirable response at 0° incidence, displaying the steepest transition at the cutoff wavelength, which is crucial for maximizing current matching in the GaInP/Si system.

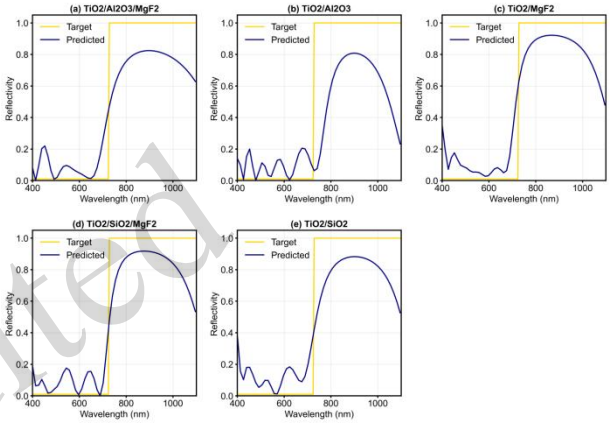

Fig. 9. Performance comparison of five models trained with distinct material configurations: For the GaInP/Si SSPV system task. The reflectance spectra at an incident angle of 0 degrees for (a) TiO_2-Al_2O_3-MgF_2 (TAM2), (b) TiO_2-Al_2O_3 (TA2), (c) TiO_2-MgF_2 (TM2), (d) TiO_2-SiO_2-MgF_2 (TSM2), and (e) TiO_2-SiO_2 (TS2).

The J-V curves of the GaInP/Si system at 0° incidence (Fig. 10) mirror the general trends observed in the GaAs/Si system. Specifically, the least impact on the GaInP cell's short-circuit current is seen in configurations TM2 and TSM2. This is a direct validation of the previous spectral analysis, confirming that the steepest band edge transition achieved by filters TM2 and TSM2 leads to minimal photon loss in the passband. The TM2 configuration achieves the highest total power density of 0.0239 W/cm^2 at 0° incidence, representing a remarkable relative enhancement of 41.9% compared to the standalone GaInP cell (0.0168 W/cm^2) and 46.6% compared to the standalone Si cell (0.0163 W/cm^2).

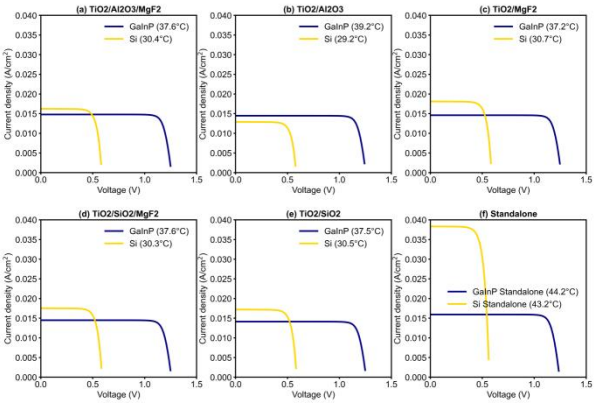

Fig. 10. J-V Curves of GaInP/Si combined solar cells under AM1.5G conditions using different spectrum splitters with a 0 degree solar incident angle to the splitters: (a) TiO_2-Al_2O_3-MgF_2 (TAM2) (b) TiO_2-Al_2O_3 (TA2) (c) TiO_2-MgF_2 (TM2) (d) TiO_2-SiO_2-MgF_2 (TSM2) (e) TiO_2-SiO_2 (TS2) (f) Standalone J-V curves of GaInP and Si as a reference.

At 45° incidence, the GaInP/Si system maintains strong performance, with the TSM2 configuration achieving the highest total power density of 0.0223 W/cm^2 (Fig. S9). This corresponds to a relative efficiency enhancement of 32.3% over standalone GaInP and 36.8% over standalone Si.

The total power density comparison for both incidence angles is presented in Fig. 11, which unequivocally validates the significant advantage of the GaInP/Si SSPV system. The total power output of all five filtered configurations exceeds that of both the standalone GaInP and Si cells at both 0° and 45° incidence, confirming the efficacy and angular robustness of the methodology.

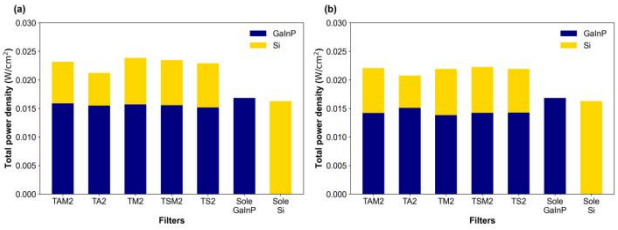

Fig. 11. Total output power density (W/cm²) of the GaInP/Si combined system using different spectral splitting filters with 0 (a) and 45 (b) degree solar incident to the splitter.

4.3.3 Thermal Performance Analysis

An important advantage of the spectral-splitting configuration is the reduction in the operating temperature of the photovoltaic cells, which directly translates to improved conversion efficiency and enhanced long-term reliability. In our thermal analysis, we assume that each PV cell reaches thermal equilibrium under illumination, with the cell temperature determined by the balance between absorbed optical power and radiative/convective heat dissipation to the ambient environment at 25°C.

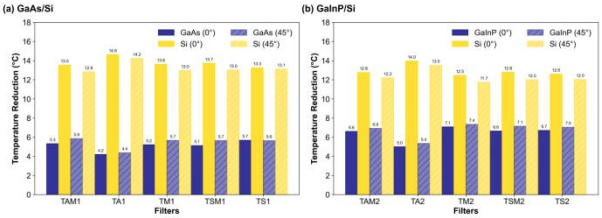

Fig. 12. Temperature reduction of the GaAs/Si (a) and GaInP/Si (b) combined system using different spectral splitting filters with 0 and 45 degree solar incident to the splitter.

The temperature reduction achieved by the spectral-splitting configuration is summarized in Fig. 12. For the GaAs/Si system (Fig. 12a), the high-bandgap GaAs cell exhibits a temperature reduction of 4.2-5.9°C at 0° incidence and 4.4-5.9°C at 45° incidence across all filter configurations. More dramatically, the low-bandgap Si cell benefits from an exceptional temperature reduction of 12.8-14.6°C at 0° incidence and 12.8-13.7°C at 45° incidence. This substantial cooling effect for the Si cell arises because it only receives the reflected long-wavelength portion of the spectrum, significantly reducing its thermal load.

For the GaInP/Si system (Fig. 12b), similar trends are observed. The high-bandgap GaInP cell achieves temperature reductions of 5.0-7.1°C at 0° incidence and 5.4-7.4°C at 45° incidence. The low-bandgap Si cell again shows the most significant benefit, with temperature reductions ranging from 11.7°C to 14.0°C at 0° incidence and 12.0°C to 13.5°C at 45° incidence. These results highlight a critical advantage of the spectral-splitting architecture: by dividing the solar spectrum between two separate cells, each cell absorbs less thermal energy than a single cell exposed to the full spectrum, resulting in substantially lower operating temperatures and consequently higher conversion efficiencies.

4.3.4 Comparison with conventional 1D PhCs

Fig. 13 compares the spectral-splitting performance of the PINN-designed TM2 photonic crystal against conventional 1D PhC structures from

the literature, encompassing both reflective/transmissive and reflective/absorptive configurations. In the short-wavelength region, the TM2 design demonstrates substantially lower reflectance intensity (predominantly below 0.1) compared to previous works 2 and 3, which exhibit reflectance values exceeding 0.1, indicating superior optical discrimination. The spectral transition at the cutoff wavelength is considerably sharper than that observed in previous work 1, while in the long-wavelength region, the reflectance remains comparable to existing designs, albeit with a modest decrease beyond 1000 nm.

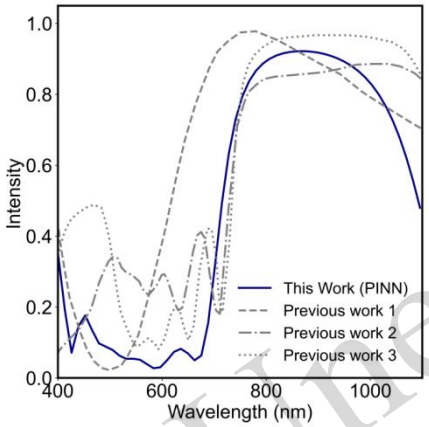

Fig. 13. Comparison of the solar spectral-splitting performance between this work's PhC (TM2), optical coating (previous work 1) from the literature (Wei et al., 2025) and 1D PhCs (previous work 2 and 3) from the literature (Wei et al., 2021).

5 Conclusions

In this study, we introduced a highly efficient, material-aware inverse design framework for 1D-PhCs based on PINNs. By embedding a differentiable TMM as a physical constraint, our method circumvents the need for large labeled datasets and enables rapid design directly from target spectra. Our key innovation lies in the MOPE approach, where a library of PINN models, each specializing in a different material combination, is pretrained. This paradigm shifts the inverse design process from simple structural optimization to a more powerful, material-aware inverse design. analysis demonstrated that the PINN model significantly outperforms a traditional data-driven CNN, reducing the validation loss by 54.5% while converging much faster. The practical power of the MOPE framework was showcased by designing a spectral-splitting filter for a tandem PV system. By deploying five pretrained material-specific models, we rapidly compared design outcomes and identified the optimal material system that maximized the PV power output, achieving total relative efficiency enhancements of 22.4% and 41.9% compared with standalone GaAs and GaInP cells, respectively. The designed filters demonstrate exceptional angular robustness, maintaining over 20% relative efficiency improvement even at 45° oblique incidence with merely 3.5% performance degradation, and effectively reduce the operating temperature of low-bandgap cells by 12.8–14.6°C, thereby enhancing long-term reliability. This result highlights the MOPE framework's capability to solve complex, real-world engineering problems efficiently. While the current demonstration focuses on conventional low-loss dielectrics to establish a fabrication-friendly baseline, we acknowledge that the bandwidth of pure Bragg reflectors is fundamentally constrained by the available refractive index contrast and the absence of resonant phase accumulation. To transcend these limitations, future iterations of the MOPE framework will integrate "expert" models for plasmonic metamaterials, lossy or dispersive nanocomposites, and high-index-contrast metasurfaces.

Acknowledgement

This work is supported by the National Natural Science Foundation of China (Grant No. 52576233) and Shenzhen Science and Technology Program (KCXST20221021111609024, KCXFZ20211020165004006, JCYJ20220818103010021).

Author contributions

Haoming Li designed the research. Zhiyuan Zhou, Wuyong Qu, and Xinzi Lin processed the corresponding data. Haoming Li wrote the first draft of the manuscript. Dongxu Ji helped to organize the manuscript. Dongxu Ji and Haoming Li revised and edited the final version.

Conflict of interest

Haoming Li, Zhiyuan Zhou, Xinzi Lin, Wuyong Qu, and Dongxu Ji declared that they have no conflict of interest.

Declaration on the use of generative AI tools

During the preparation of this work, the authors used ChatGPT and Gemini to improve language and readability. After using these tools, the authors reviewed and edited the content as needed and take full responsibility for the content

of the publication.

Data availability

The data that support the findings of this study are available from the corresponding author upon reasonable request.

Reference

Ahmadi M, Pagano R, Matera F, et al., 2025. Analysis of light collection in GaAs/Si HJT four-terminal solar cell system based on spectral splitting and polymeric wedged optics: a role for diffusive lateral supports. *Solar Energy,* Vol. 301113934.

Anzengruber S W, Klann E, Ramlau R, et al., 2012. Numerical methods for the design of gradient-index optical coatings. *Applied Optics,* Vol. 51 No. 34, pp. 8277-8295.

Chen Y, Dal Negro L, 2022. Physics-informed neural networks for imaging and parameter retrieval of photonic nanostructures from near-field data. *APL Photonics,* Vol. 7 No. 1, pp. 010802.

Chen Y, LU L, Karniadakis G E, et al., 2020. Physics-informed neural networks for inverse problems in nano-optics and metamaterials. *Optics Express,* Vol. 28 No. 8, pp. 11618-11633.

Dorodnyy A, Shklover V, Braginsky L, et al., 2015. High-etfficiency spectrum splitting for solar photovoltaics. *Solar Energy Materials and Solar Cells,* Vol. 136120-126.

Hecht E, 2021. Optics Fifth Edition, London, Pearson.

Hong Y, Nicholls D P, 2022. Data-driven design of thin-film optical systems using deep active learning. *Optics Express,* Vol. 30 No. 13, pp. 22901-22910.

I Ahmed, Jeon G, Piccialli F, 2022. From Artificial Intelligence to Explainable Artificial Intelligence in Industry 4.0: A Survey on What, How, and Where. *IEEE Transactions on Industrial Informatics,* Vol. 18 No. 8, pp. 5031-5042.

Jiang Y, Keevers M J, Pearce P, et al., 2019. Design of an intermediate Bragg reflector within triple-junction solar cells for spectrum splitting applications. *Solar Energy Materials and Solar Cells,* Vol. 193259-269.

Jiménez-Luna J, Grisoni F, Schneider G, 2020. Drug discovery with explainable artificial intelligence. *Nature Machine Intelligence,* Vol. 2 No. 10, pp. 573-584.

Khatib O, Ren S, Malof J, et al., 2022. Learning the Physics of All-Dielectric Metamaterials with Deep Lorentz Neural Networks. *Advanced Optical Materials,* Vol. 10 No. 13, pp. 2200097.

Kim M, Seo J,Yoon S,et al.,2021.Optimization and performance analysis of a multilayer structure for daytime radiative cooling. *Journal of Quantitative Spectroscopy and Radiative Transfer*,260,107475.

Lee I, Kim C, Ju K, et al., 2023. Implementation of particle swarm optimization for complete inverse design of multilayered optical filters. *Applied Optics,* Vol. 62 No. 34, pp. 8994-9001.

Li H, Wan S, Wang L, et al., 2025. Divide and conquer: Spectral-splitting and utilization of thermal radiation from waste heat in the steel industry. *Applied Energy,* Vol. 378124836.

Li J, Jiang Y, Liu J, et al., 2024. A photosynthetically active radiative cooling film. *Nature Sustainability,* Vol. 7 No. 6, pp. 786-795.

Lininger A, Hinczewski M, Strang G, 2021. General Inverse Design of Layered Thin-Film Materials with Convolutional Neural Networks. *ACS Photonics,* Vol. 8 No. 12, pp. 3641-3650.

Liu D, Tan Y, Khoram E, et al., 2018. Training Deep Neural Networks for the Inverse Design of Nanophotonic Structures. *ACS Photonics,* Vol. 5 No. 4, pp. 1365-1369.

Liu G, Chen S, Lin C, 2024. Optimization of Dielectric-Metal Multilayer Structure for Color-Preserving Radiative Cooling Window. *ACS Omega,* Vol. 9 No. 28, pp. 30425-30435.

Luce A, Mahdavi A, Marquardt F, et al., 2022. TMM-Fast, a transfer matrix computation package for multilayer thin-film optimization: tutorial. *Journal of the Optical Society of America A,* Vol. 39 No. 6, pp. 1007-1013.

Luce A, Mahdavi A, Wankerl H, et al., 2023. Investigation of inverse design of multilayer thin-films with conditional invertible neural networks. *Machine Learning: Science and Technology,* Vol. 4 No. 1, pp. 015014.

Ma T, Wang H, Guo L, 2024. OptoGPT: A foundation model for inverse design in optical multilayer thin film structures. *Opto-Electronic Advances,* Vol. 7 No. 7, pp. 240062-1-240062-13.

Ma X, Li X, Wang Y, 2025. One-dimensional Si/SiO2 photonic crystal filters for GaxIn1-xAsySb1-y thermophotovoltaic devices. *Journal of the Optical Society of America B,* Vol. 42 No. 12, pp. 2740-2746.

Medvedev V, Erdmann A, Rosskopf A, 2025. Physics-informed deep learning for 3D modeling of light diffraction from optical metasurfaces. *Optics Express,* Vol. 33 No. 1, pp. 1371-1384.

Molesky S, LIN Z, Piggott A Y, et al., 2018. Inverse design in nanophotonics. *Nature Photonics,* Vol. 12 No. 11, pp. 659-670.

Pavlichenko I, Broda E, Fukuda Y, et al., 2015. Bringing one-dimensional photonic crystals to a new light: an electrophotonic platform for chemical mass transport visualisation and cell monitoring. *Materials Horizons,* Vol. 2 No. 3, pp. 299-308.

Pedreschi D, Giannotti F, Guidotti R, et al., 2019. Meaningful Explanations of Black Box AI Decision Systems. *Proceedings of the AAAI Conference on Artificial Intelligence,* Vol. 33 No. 01, pp. 9780-9784.

Qian C, Tan S, Li E, et al., 2024. Driving deep-learning-based metasurface design with Kramers-Kronig relations. *Physical Review Applied,* Vol. 22 No. 4, pp. L041002.

Qu W, Li H, Li G, et al., 2025. Genetic algorithm-driven design of a spectral-splitting filter for a high-efficiency

hybrid photovoltaic-thermoelectric system. *Case Studies in Thermal Engineering,* Vol. 75107255.

Rahman R U, Yousuf H, Khokhar M Q, et al., 2025. Optimized current and voltage matching in high-efficiency bifacial III − V/silicon multijunction solar cells with enhanced spectral albedo. *Sustainable Energy Technologies and Assessments,* Vol. 77104332.

Riganti R, ZHU Y, CAI W, et al., 2025. Multiscale Physics-Informed Neural Networks for the Inverse Design of Hyperuniform Optical Materials. *Advanced Optical Materials,* Vol. 13 No. 16, pp. 2403304.

Ruan Z, Yuan Y, Zhang X, et al., 2016. Determination of optical properties and thickness of optical thin film using stochastic particle swarm optimization. *Solar Energy,* Vol. 127147-158.

Rühle S, 2016. Tabulated values of the Shockley–Queisser limit for single junction solar cells. *Solar Energy,* Vol. 130139-147.

Schubert M F, Mont F W, Chhajed S, et al., 2008. Design of multilayer antireflection coatings made from co-sputtered and low-refractive-index materials by genetic algorithm. *Optics Express,* Vol. 16 No. 8, pp. 5290-5298.

Tikhonravov A V, Trubetskov M K, Debell G W, 1996. Application of the needle optimization technique to the design of optical coatings. *Applied Optics,* Vol. 35 No. 28, pp. 5493-5508.

Tikhonravov A V, Trubetskov M K, Debell G W, 2007. Optical coating design approaches based on the needle optimization technique. *Applied Optics,* Vol. 46 No. 5, pp. 704-710.

Wan B, Zhou Z, Xu Y, et al., 2021. A Theoretical Proposal for a Refractive Index and Angle Sensor Based on One-Dimensional Photonic Crystals. *IEEE Sensors Journal,* Vol. 21 No. 1, pp. 331-338.

Wang H, Zheng Z, Ji C, et al., 2021. Automated multi-layer optical design via deep reinforcement learning. *Machine Learning: Science and Technology,* Vol. 2 No. 2, pp. 025013.

Wang J, Li Y, Gao R, et al., 2022. Hybrid physics-based and data-driven models for smart manufacturing: Modelling, simulation, and explainability. *Journal of Manufacturing Systems,* Vol. 63381-391.

Wang Q, Zhang Y, Burguete-Lopez A, et al., 2024. The transformational dive of nanophotonics inverse design from deep learning to artificial general intelligence. *APL Photonics,* Vol. 9 No. 10, pp. 100902.

Wei D,Cao F,Wu Z,et al.,2021.Enhanced spectral splitting in a novel solar spectrum optical splitter based on one dimensional photonic crystal heterostructure.Journal of Materiomics,7,648-655.

Wei R,Xu T,Guo C,2025.High-Efficiency Solar Hybrid Photovoltaic/Thermal System Enabled by Ultrathin Asymmetric Fabry–Perot Cavity.ACS Photonics,12,628-635.

Yu T, Liu R, Yang Z, et al., 2025. Color Design for Daytime Radiative Cooling: Fundamentals and Approaches. *Applied Energy,* Vol. 377124436.

Yu Z, Fisher K C, Wheelwright B M, et al., 2015. PVMirror: A New Concept for Tandem Solar Cells and Hybrid Solar Converters. *IEEE Journal of Photovoltaics,* Vol. 5 No. 6, pp. 1791-1799.

Zhan T, Liu Q, SUN Y, et al., 2022. A general machine learning-based approach for inverse design of one-dimensional photonic crystals toward targeted visible light reflection spectrum. *Optics Communications,* Vol. 510127920.

Zhelyeznyakov M, Fröch J, Wirth-Singh A, et al., 2023. Large area optimization of meta-lens via data-free machine learning. *Communications Engineering,* Vol. 2 No. 1, pp. 60.

Zhu L, Lv C, Hua W, et al., 2025. PTLOR-Net: Physical Transfer Learning Based Optical Response Prediction Network of Metasurfaces. *ACS Photonics,* Vol. 12 No. 5, pp. 2624-2636.

Electronic supplementary materials

Section S1-S12, Table S1-S2, Figs. S1-S9

中文概要

题　　目：材料自适应的一维光子晶体快速逆向设计方法：混合物理专家模型

作　　者：李浩铭，周致远，林馨姿，屈武永，纪冬旭

机　　构：香港中文大学（深圳），理工学院，中国深圳，518172

目　　的：传统一维光子晶体逆向设计方法计算成本高、依赖大量标注数据且无法优化材料选择。本文旨在提出一种基于物理信息神经网络（PINN）的快速材料感知逆向设计框架，实现从目标光谱直接进行结构优化与材料系统筛选。

创新点：1. 提出混合物理专家（MOPE）框架，预训练多种材料组合的 PINN 模型库，实现材料系统的快速选择与结构并行优化；2. 将可微分传输矩阵法嵌入 PINN 损失函数作为物理约束，消除对大量标注数据的依赖；3. 实现从目标光谱（含手绘光谱）直接快速逆向设计，并拓展至光谱分光光伏系统的实际工程应用。

方　　法：1. 构建可微分传输矩阵法（TMM）作为 PINN 训练的物理前向模型与损失约束；2. 预训练八种材料组合的 PINN 专家模型，通过并行推理比较设计结果以筛选最优材料配置；3. 将 MOPE 框架应用于 GaAs/Si 和 GaInP/Si 光谱分光光伏系统的分光滤波器设计，评估

系统输出功率、角向鲁棒性及热管理性能。

结　　论： 1. PINN 验证损失较数据驱动 CNN 降低 54.5%，且收敛速度显著提升；2. TiO_2-SiO_2材料组合在可见光波段逆向设计任务中综合表现最优；3. 光谱分光系统整体效率较独立 GaAs 电池提升 22.4%，较 GaInP 电池提升 41.9%；4. 设计滤波器具有优异的角向鲁棒性，45°斜入射时相对效率仅下降 3.5%；5. 低带隙电池工作温度降低 12.8–14.6°C，有效提升系统转换效率与长期可靠性。

关键词： 光子晶体；物理信息神经网络；混合专家模型；逆向设计；光谱分光光伏